High Reynolds number calculations using the dynamic subgrid-scale stress model

Ugo Piomelli

Articles you may be interested in

High Reynolds number calculations using the dynamic subgrid-scale stress model

Ugo Piomelli

Department of Mechanical Engineering, University of Maryland, College Park, Maryland 20742

The dynamic subgrid-scale eddy viscosity model has been used in the large-eddy simulation of the turbulent flow in a plane channel for Reynolds numbers based on friction velocity and channel half-width ranging between 200 and 2000, a range including values significantly higher than in previous simulations. The computed wall stress, mean velocity, and Reynolds stress profiles compare very well with experimental and direct simulation data. Comparison of higher moments is also satisfactory. Although the grid in the near-wall region is fairly coarse, the results are quite accurate: the turbulent kinetic energy peaks at $y^+ \simeq 12$, and the near-wall behavior of the resolved stresses is captured accurately. The model coefficient is $o(10^{-3})$ in the buffer layer and beyond, where the cutoff wave numbers are in the decaying region of the spectra; in the near-wall region the cutoff wave numbers are nearer the energy-containing range, and the resolved turbulent stresses become a constant fraction of the resolved stresses. This feature is responsible for the correct near-wall behavior of the model coefficient. In the near-wall region the eddy viscosity is reduced to account for the energy transfer from small to large scales that may occur locally.

I. INTRODUCTION

Renewed interest has been focused in the past few years on the use of large-eddy simulation (LES) for the prediction of turbulent and transitional flow fields. In LES only the large, energy-containing, scales are resolved; the small, subgrid scales, whose effect appears through a residual stress term, are modeled. Since the subgrid scales tend to be more homogeneous and isotropic than the large ones, and are responsible for only a fraction of the momentum and energy transport, their modeling is easier than the modeling of all scales of motion required in Reynolds-averaged calculations, and the numerical results tend to be less dependent on the accuracy of the model. Moreover, since only the large scales of motion must be resolved, LES requires less computational effort than the direct numerical simulation (DNS) of the Navier–Stokes equations. LES has been successfully applied to the study of various transitional and turbulent flows (see Ref. 1 for an overview of recent applications of LES in engineering flows).

A subgrid-scale stress model that has recently received considerable attention is the dynamic eddy viscosity model;[2] its main feature is the fact that the model coefficient is calculated, rather than input *a priori*. The dynamic eddy viscosity model requires the use of two filters, the *grid filter* and the *test filter*, and uses information on the energy content of the smallest resolved scales (whose wavelength is intermediate between the two filter widths) to determine the model coefficient. This results in a coefficient that can vary with position and time, and that vanishes in laminar flows or near solid boundaries with the correct asymptotic behavior. The model can also predict subgrid-scale backscatter (transfer of energy from the small to the large scales of motion).

Although in principle the coefficient is a function of space and time, in practical applications it is usually assumed that it only varies with time and with the spatial coordinates in the inhomogeneous directions. This assumption, which is required to eliminate ill-conditioning that was found to occur whenever the denominator of the expression giving the model coefficient became very small or negative,[2] limits the range of applicability of the model in its present form to flows with at most two directions of inhomogeneity. Efforts to develop local versions of the model are presently underway.[3]

This model has been used to compute transitional and turbulent channel flows,[2,4] compressible flows,[5] and flows with passive scalars.[6] Lilly[7] suggested an improved way to determine the coefficient, which yields more accurate results than the original formulation.[6] Wong[8] proposed dynamic isotropic and anisotropic one-equation subgrid-scale stress models, and Ronchi and co-workers[9] have examined some of the assumptions used to obtain the model, and pointed out some possible difficulties in the model implementation.

In this work, the dynamic model will be used to compute the turbulent flow in a plane channel at high Reynolds number. These simulations will serve various purposes: first, they will test the accuracy of the model in calculations in which a significant percentage of the energy is in the subgrid scales and the grid resolution in the near-wall region is necessarily marginal. In the past, high Reynolds number LES calculations used approximate boundary conditions to bypass the wall region altogether;[10,11] the present ones are the first simulations that attempt to resolve the wall layer at Reynolds numbers (based on friction velocity and channel half-width) of the order of 2000. Second, the simulation results will be used to determine how having grid and test filter widths in the dissipative, inertial, or energy-containing ranges of the spectrum affects the accuracy of the numerical results. Finally, they will be used to investigate the model behavior in the near-wall region, and

the effect of under resolution of the wall-layer structures on the LES results.

In the next section the problem will be formulated, and the model and numerical scheme used will be described. Then, in Sec. III, the simulation results will be presented and discussed. Final comments will be made in Sec. IV.

II. PROBLEM FORMULATION

In large-eddy simulations the flow variables are decomposed into a large scale (or resolved) component, denoted by an overbar, and a subgrid-scale component. The large-scale component is defined by the filtering operation:

$$\bar{f}(\mathbf{x}) = \int_D \bar{G}(\mathbf{x},\mathbf{x}')f(\mathbf{x}')d\mathbf{x}', \qquad (1)$$

where the integral is extended over the entire domain D and $\bar{G}$ is the grid filter function. The length scale associated with $\bar{G}$ is the filter width $\bar{\Delta}$.

The filtered Navier–Stokes and continuity equations, which describe the evolution of the large, energy-carrying eddies, can be obtained by applying the filtering operation to the incompressible Navier–Stokes and continuity equations to yield

$$\frac{\partial \bar{u}_i}{\partial t} + \frac{\partial}{\partial x_j}(\bar{u}_i\bar{u}_j) = -\frac{\partial \bar{p}}{\partial x_i} - \frac{\partial \tau_{ij}}{\partial x_j} + \frac{1}{\mathrm{Re}_\tau}\frac{\partial^2 \bar{u}_i}{\partial x_j \partial x_j}, \qquad (2)$$

$$\frac{\partial \bar{u}_i}{\partial x_i} = 0, \qquad (3)$$

in which the channel half-width δ and the friction velocity $u_\tau = (\tau_w/\rho)^{1/2}$ are used to make the equations dimensionless and to define the Reynolds number Re_τ, and τ_w is the shear stress at the wall.

The dynamic eddy viscosity model parametrizes the anisotropic part of the subgrid-scale (SGS) Reynolds stresses, $\tau_{ij} = \overline{u_i u_j} - \bar{u}_i\bar{u}_j$, by an eddy viscosity assumption

$$\tau_{ij} - \frac{\delta_{ij}}{3}\tau_{kk} = -2\nu_T\bar{S}_{ij} = -2C(y,t)\bar{\Delta}^2|\bar{S}|\bar{S}_{ij}, \qquad (4)$$

in which δ_{ij} is Kronecker's delta, and $|\bar{S}| = \sqrt{2\bar{S}_{ij}\bar{S}_{ij}}$ is the magnitude of the large-scale strain rate tensor

$$\bar{S}_{ij} = \frac{1}{2}\left(\frac{\partial \bar{u}_i}{\partial x_j} + \frac{\partial \bar{u}_j}{\partial x_i}\right); \qquad (5)$$

the subgrid-scale kinetic energy $q_{\mathrm{SGS}}^2 = \tau_{kk}$ is added to the pressure term. If a second filter, the test filter $\hat{G}$, is defined, one can exploit the identity[12]

$$\mathcal{L}_{ij} = T_{ij} - \hat{\tau}_{ij}, \qquad (6)$$

which relates the resolved turbulent stresses $\mathcal{L}_{ij} = \widehat{\bar{u}_i\bar{u}_j} - \hat{\bar{u}}_i\hat{\bar{u}}_j$, the subgrid-scale stresses τ_{ij}, and the subtest-scale stresses $T_{ij} = \widehat{u_i u_j} - \hat{\bar{u}}_i\hat{\bar{u}}_j$, to determine the coefficient $C(y,t)$. If the subtest stresses are parametrized, in a manner analogous to the subgrid ones, by

$$T_{ij} - \frac{\delta_{ij}}{3}T_{kk} = -2C(y,t)\hat{\bar{\Delta}}^2|\hat{\bar{S}}|\hat{\bar{S}}_{ij} \qquad (7)$$

Case	Grid	Re_τ	Re_c	Grid spacing
1	48×65×64	200	3800	$\Delta x^+ = 53$; $10 > \Delta y^+ > 0.24$; $\Delta z^+ = 13$
2	96×97×96	1050	23 700	$\Delta x^+ = 86$; $32 > \Delta y^+ > 0.53$; $\Delta z^+ = 17$
3	48×65×64	1050	23 700	$\Delta x^+ = 172$; $51 > \Delta y^+ > 1.25$; $\Delta z^+ = 26$
4	64×81×80	2000	47 100	$\Delta x^+ = 244$; $77 > \Delta y^+ > 1.50$; $\Delta z^+ = 40$

(where $\hat{\bar{\Delta}}$ and $\hat{\bar{S}}_{ij}$ are, respectively, the length scale and large-scale strain rate tensors associated with the test filter $\hat{G}$), and (4) and (7) are substituted into (6), requiring that the error be minimized in the least-squares sense[7] gives

$$C(y,t) = -\frac{1}{2}\frac{\langle \mathcal{L}_{ij}M_{ij}\rangle}{\langle M_{ij}M_{ij}\rangle}, \qquad (8)$$

where $\langle \ \rangle$ denotes averaging over a plane parallel to the wall, and

$$M_{ij} = \hat{\bar{\Delta}}^2|\hat{\bar{S}}|\hat{\bar{S}}_{ij} - \bar{\Delta}^2\widehat{|\bar{S}|\bar{S}_{ij}}. \qquad (9)$$

In the present work the subgrid-scale stresses are modeled by (4), with the coefficient $C(y,t)$ given by (8). The single model parameter is the ratio of the filter widths, $\hat{\bar{\Delta}}/\bar{\Delta}$. Following Germano et al.,[2] $\hat{\bar{\Delta}}_1 = 2\bar{\Delta}_1$, $\hat{\bar{\Delta}}_2 = \bar{\Delta}_2$, $\hat{\bar{\Delta}}_3 = 2\bar{\Delta}_3$, and

$$\bar{\Delta}^3 = \bar{\Delta}_1\bar{\Delta}_3\bar{\Delta}_3; \quad \hat{\bar{\Delta}}^3 = \hat{\bar{\Delta}}_1\hat{\bar{\Delta}}_3\hat{\bar{\Delta}}_3. \qquad (10)$$

The sharp Fourier cutoff is used as both grid and test filter in the x and z directions, and truncation in Chebyshev space is used as the grid filter in the y direction; no test filtering is performed in y.

The governing equations (2) and (3) are integrated in time using a Fourier–Chebyshev pseudospectral collocation scheme.[13] The skew-symmetric form of the momentum equation (2) is employed, and the time advancement is performed by a fractional time step method with a semi-implicit scheme; the wall-normal diffusion term is advanced using the Crank–Nicolson scheme, and the remaining terms by a low-storage third-order Runge–Kutta scheme. Periodic boundary conditions are applied in the streamwise (x) and spanwise (z) directions, and no-slip conditions at the solid walls, which are located at $y = \pm 1$. No dealiasing is performed.

All simulations were started from a realization of the flow at either a lower Reynolds number, or on a coarser grid, and the equations were integrated in time until steady state was reached. Then statistics were accumulated (typically over times $tu_\tau/\delta = 2$ to 4).

III. RESULTS AND DISCUSSION

Four calculations were performed, at three Reynolds numbers varying between 200 and 2000. Table I, in which Re_c is the Reynolds number based on centerline velocity U_c and channel half-width δ, summarizes the various cases. The size of the computational domain was $L_x = 4\pi\delta$, $L_z = \pi\delta$ for the low Reynolds number case (case 1) and $L_x = 5\pi\delta/2$, $L_z = \pi\delta/2$ for the others. The dimensions cho-
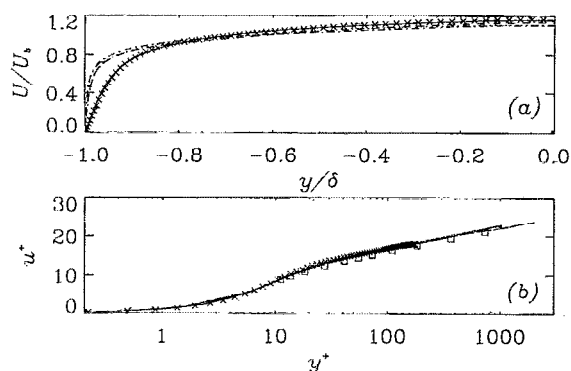
FIG. 1. Mean velocity. ——: Case 1; ····: case 2; – – –: case 3; – · –: case 4; ×: DNS (Ref. 14); □: experiment (Ref. 16). (a) Global coordinates; (b) wall coordinates.

FIG. 2. Turbulence intensities in global coordinates. ——: Case 1; ····: case 2; – – –: case 3; – · –: case 4; ×: DNS (Ref. 14); △: experiment (Ref. 15). (a) u''; (b) v''; (c) w''.

sen are sufficient to contain the largest structures present in the flow, as confirmed *a posteriori* by an examination of the two-point correlations.

Case 1 is a high-resolution, low Reynolds number calculation in which the subgrid-scale contribution to the energy and Reynolds stress is fairly small (the mean subgrid-scale Reynolds shear stress is less than 20% of the large-scale one everywhere). Cases 2 and 3 are at a Reynolds number, $Re_\tau = 1050$, for which experimental data are available. These two simulations can also provide indications on the effects of grid resolution effects. Finally, case 4 is a low-resolution simulation at very high Reynolds number, $Re_\tau \simeq 2000$ ($Re_c = 47\,100$). Previous calculations in which the wall layer was resolved typically studied the range $Re_\tau \simeq 200-650$, and the only computations of flows with $Re_c \simeq 50\,000$ performed up to now used approximate boundary conditions.[10,11]

The LES results will be compared with direct simulation and experimental data. The DNS data is from the plane channel simulation of Kim *et al.*[14] at $Re_\tau = 180$. The experimental data of Wei and Willmarth[15] for plane channel flow at $Re_c = 23\,000$, and the boundary-layer data of Balint *et al.*[16] at $Re_\delta = 28\,000$ (based on free-stream velocity and boundary-layer thickness) will be compared with cases 2 and 3.

Mean velocity profiles for the various cases are shown in Fig. 1. In Fig. 1(a) the velocity is normalized by the bulk velocity

$$U_b = \frac{1}{2} \int_{-1}^{1} U \, dy, \qquad (11)$$

where $U_i = \langle \bar{u}_i \rangle$ and $\langle \ \rangle$ now denotes long-time averaging. All calculations exhibit a logarithmic layer with a von Kármán constant $\kappa = 0.4$, and an intercept $A = 5.5$ for case 1 and $A = 5.2$ for all the other cases, in good agreement with accepted values. The wall stress was always within 5% of the correlation of experimental data.[17]

The rms intensities of the large-scale turbulent fluctuations $u_i'' = \bar{u}_i - U_i$ are compared in Figs. 2 and 3 with the DNS and experimental data. The agreement between the LES results and the DNS and experimental data is uni-
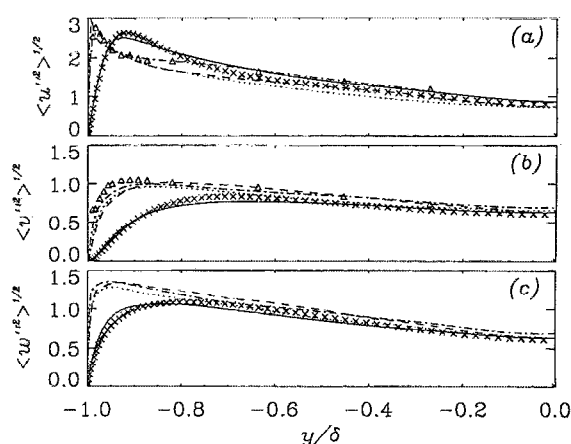
formly good, with no loss of accuracy in the near-wall region even at the highest Reynolds number. The location and magnitude of the peak streamwise turbulence intensity are predicted correctly even in the low-resolution calculation. Little difference can be observed between the results of cases 2 and 3, which are at the same Reynolds number but with different meshes.

The mean shear stress $\langle \tau_{12} \rangle$ in the near-wall region is shown in Fig. 4. The agreement of case 1 results with the DNS data is very good (notice in particular the near-wall behavior of the large-scale stresses). In cases 2 and 3, however, the LES data are higher than the experimental results; Wei and Willmarth[15] obtained Reynolds shear stress profiles using two methods: the direct measurements of the u and v fluctuations (shown in the figure), and closure of the mean momentum equation in the streamwise direction. At the Reynolds number under consideration the two methods gave results that differed considerably for $y^+ < 70$, direct measurements yielding lower values than the mo-
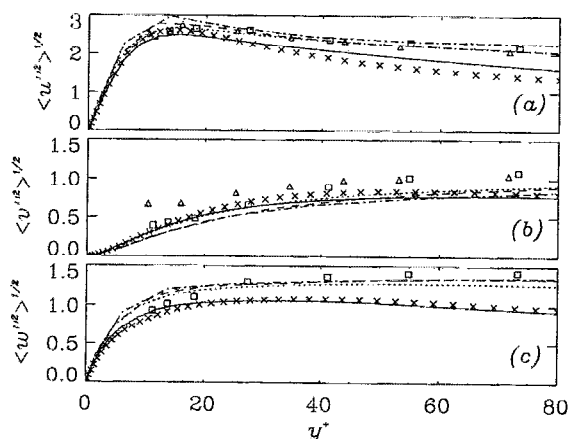

FIG. 3. Turbulence intensities in wall coordinates. ——: Case 1; ····: case 2; – – –: case 3; – · –: case 4; ×: DNS (Ref. 14); △: experiment (Ref. 15); □: experiment (Ref. 16). (a) u''; (b) v''; (c) w''.
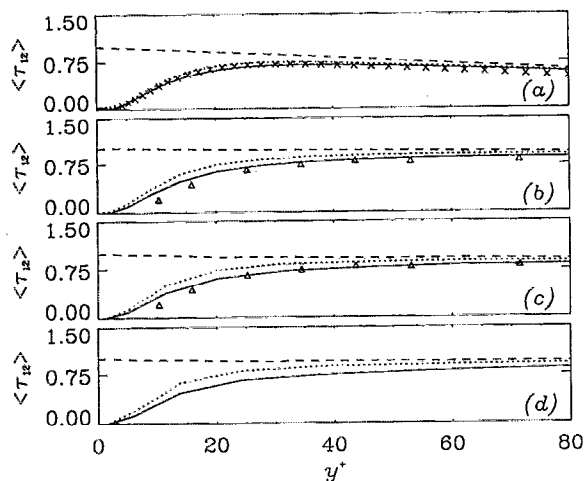
FIG. 4. Shear stress in wall coordinates. ——: Large-scale; ⋯⋯: large-scale+SGS; − − −: total; ×: DNS (Ref. 14); △: experiment (Ref. 15). (a) Case 1; (b) case 2; (c) case 3; (d) case 4.

FIG. 6. Flatness factor in wall coordinates. ——: Case 1; ⋯⋯: case 2; − − −: case 3; − · −: case 4; ×: DNS (Ref. 14); □: experiment (Ref. 16). (a) $F(u)$; (b) $F(v)$; (c) $F(w)$.

mentum balance. At $y^+ = 10$, for example, the direct measurements gave a normalized shear stress $\langle -u'v' \rangle \simeq 0.2$, whereas the momentum balance method gave $\langle -u'v' \rangle \simeq 0.5$, in much better agreement with the LES value of 0.52. Wei and Willmarth[15] attribute the discrepancy between the results of the two techniques to insufficient resolution of the laser-Doppler measurements.

The skewness and flatness factors of the large-scale velocity are shown in Figs. 5 and 6. The skewness of w is nearly zero, as required by the spanwise symmetry of the flow; the skewness of v is in good agreement with DNS and experimental data; it is negative for $5 < y^+ < 30$, reflecting the presence of strong negative v motions there.[14] The skewness of u requires some discussion; the low Reynolds number, high-resolution case is in good agreement with the DNS data, and cases 2 and 3 are in good agreement with the experimental data for $y^+ > 20$. With increasing Reynolds number $S(u)$ increases, and the region where $S(v)$ is
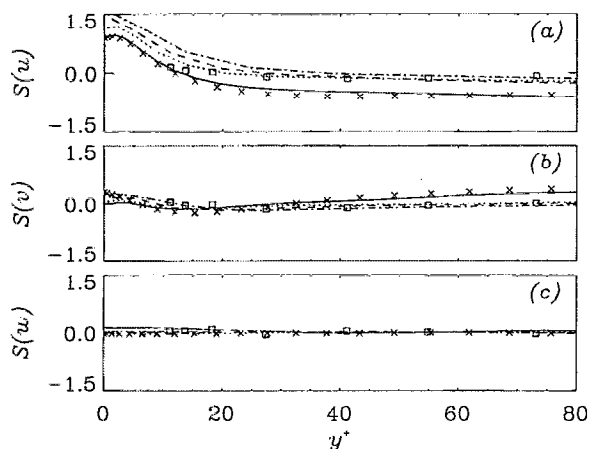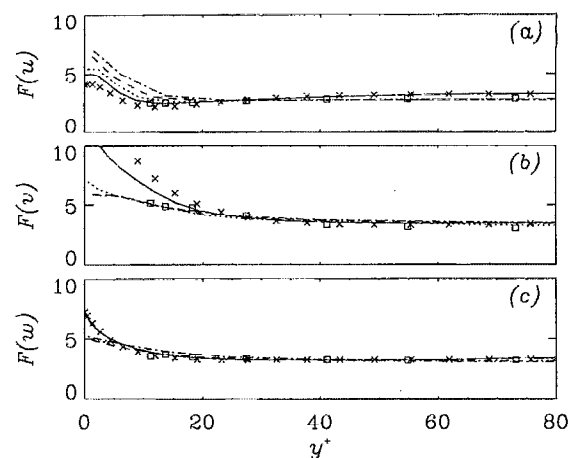

FIG. 5. Skewness factor in wall coordinates. ——: Case 1; ⋯⋯: case 2; − − −: case 3; − · −: case 4; ×: DNS (Ref. 14); □: experiment (Ref. 16). (a) $S(u)$; (b) $S(v)$; (c) $S(w)$.

negative moves away from the wall, trends also observed in the experiments. It must be remarked here that since in LES only the large-scale velocity is computed, perfect agreement of LES statistics with experimental data should not be expected, unless the contribution of the subgrid scales can be estimated. The SGS contribution to the shear stress can be evaluated, but not the SGS contribution to higher-order moments; since the small scales tend to be more homogeneous and isotropic than the large ones, however, they should decrease the skewness. This conjecture is supported by the comparison of cases 2 and 3, and of the DNS results with case 1: the coarser grid calculations have a slightly higher skewness than the more finely resolved ones. It is not known whether the contribution of the subgrid scales to the skewness would be sufficient to completely cancel the increasing trend. The flatness of u [Fig. 6(a)] shows a trend similar to that discussed before. The flatness factors of v and w, on the other hand, decrease in the near-wall region with increasing Reynolds number; the LES results agree well with the experiments, but both LES and experiments could be affected by insufficient resolution, particularly in the prediction (or measurement) of v fluctuations.

The one-dimensional spectra of the large-scale turbulent kinetic energy $q^2 = u_i'' u_i''$ at two y locations in the channel are shown in Fig. 7 for cases 2 and 3. Good agreement is observed between the two calculations, although energy piles up near the cutoff wave number in the coarse calculation for $y^+ < 20$. The streamwise cutoff wave numbers for the grid and test filters are $\bar{K}_x = 38$ and $\hat{K}_x = 19$ for case 2, $\bar{K}_x = 19$ and $\hat{K}_x = 10$ for case 3; for $y^+ < 12$ they both lie in a region in which the slope of the spectrum is shallower than $-5/3$ (close to -0.8 at $y^+ = 12$), while at $y^+ = 300$ they are both in the inertial region. The spanwise cutoff wave numbers, $\bar{K}_z = 192$ and $\hat{K}_z = 96$ for case 2, $\bar{K}_z = 128$ and $\hat{K}_z = 64$ for case 3, are both in the inertial range at $y^+ = 12$, in the dissipation range at $y^+ = 300$.

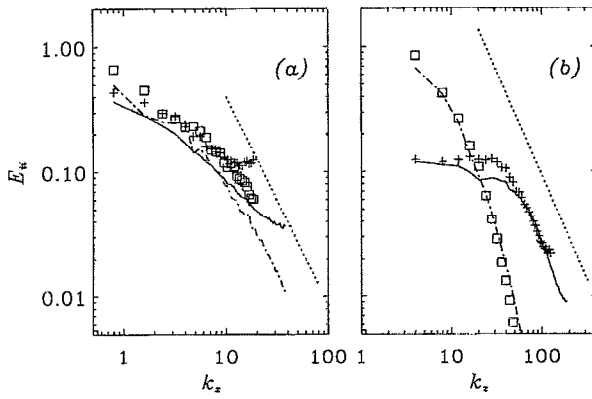When the grid and test filters are in decaying parts of

FIG. 7. One-dimensional spectra of the large-scale turbulent kinetic energy q^2 for the $Re_\tau \approx 1000$ calculations. The dotted line represents a $k^{-5/3}$ slope. ——: case 2, $y^+ = 12$; +: case 3, $y^+ = 12$; – · –: case 2, $y^+ = 300$; □: case 3, $y^+ = 300$; (a) streamwise; (b) spanwise.

FIG. 9. Contours of streamwise velocity fluctuations u'' in the $y^+ \approx 6$ plane. Dashed lines indicate positive contours. Contour levels are ± 5, ± 4, ± 3, ± 2, ± 1. (a) Case 1 ($Re_\tau = 200$); (b) case 2 ($Re_\tau = 1050$); (c) case 3 ($Re_\tau = 1050$); (d) case 4 ($Re_\tau = 2000$).

the spectrum the resolved turbulent stresses $\mathscr{L}_{ij}$ become a small percentage of the large-scale stresses $u_i'' u_j''$ [see Fig. 8(b) for the ratio $\langle \mathscr{L}_{kk} \rangle / \langle q^2 \rangle$; a similar result can be obtained for $\langle \mathscr{L}_{12} \rangle / \langle u'' v'' \rangle$]; the coefficient, however, approaches a constant value that is not very grid dependent: for $-0.8 < y < 0.8$, C varies between 0.003 and 0.004 for both grids; its average value is 0.0035 for the fine mesh, 0.0036 for the coarse one (corresponding to a Smagorinsky constant $C_s \approx 0.06$, slightly lower than the commonly used values, that range between 0.08 and 0.1). This behavior is due to a simultaneous decrease of the denominator, which contains terms like $|\hat{\bar{S}}|^3$, $|\hat{\bar{S}}| \hat{\bar{S}}_{ij} |\widehat{\bar{S}} | \bar{S}_{ij}$, and $|\bar{S}| \bar{S}_{ij} | \widehat{\bar{S}} | \bar{S}_{ij}$, that become small away from the solid boundaries.

Near the wall, on the other hand, where both filters are in flatter regions of the spectrum, $\langle \mathscr{L}_{kk} \rangle / \langle q^2 \rangle$ approaches a constant value; if the spectrum were completely flat, this value would be the ratio of test to grid cutoff wave numbers in the x-z plane (which is one-half), consistent with the data. Similar indications can be obtained from the ratio $\langle \mathscr{L}_{12} \rangle / \langle u'' v'' \rangle$.

A few remarks must be made regarding the ability of low-resolution LES calculations to capture the structure of
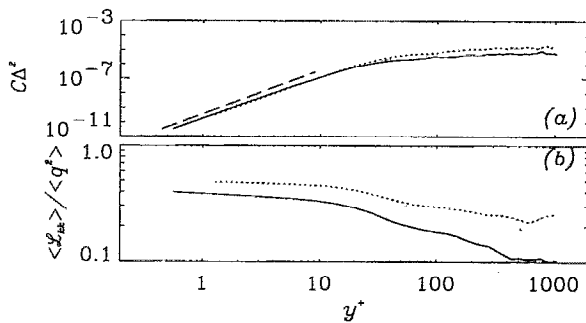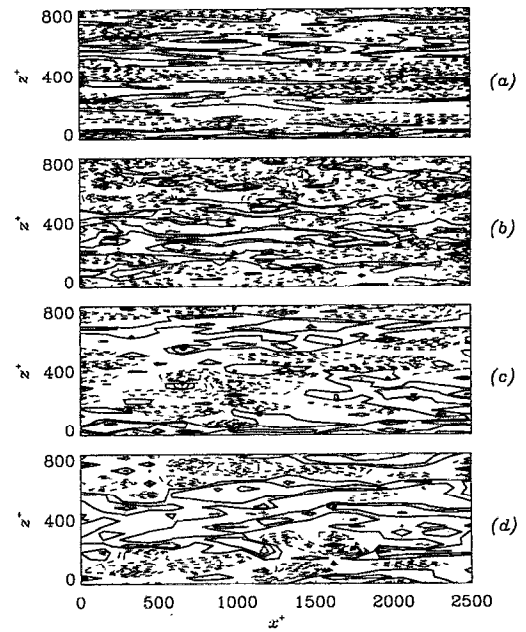
turbulence at high Reynolds numbers. Among the most important structures in the near-wall region are the low-speed streaks; the mean streak spacing in wall units, which was calculated from the two-point correlations, is, respectively, 120, 190, 210, and 310 for cases 1–4. Except for case 1, these values are larger than the experimental ones, as is usually found in LES calculations. Contours of streamwise velocity fluctuation u'' in an x-z plane near the wall are shown in Fig. 9, and contours of $u'' v''$ stress in Fig. 10. Both u'' and $u'' v''$ contours for case 1 resemble those obtained from direct simulations. As the mesh becomes coarser (in wall units), however, the structures tend to become wider and less elongated in the streamwise direction (an observation confirmed by the two-point correlations), as a result of the inadequate grid resolution at high Reynolds number. Cases 2 and 3 highlight this difference: the contours of u'' and $u'' v''$ are significantly more diffused, and fewer large Reynolds stress events are observed in case 3; the less frequent occurrence of high-intensity v fluctuations is also responsible for the decreased flatness in this region.

When the Smagorinsky model was used, inadequate resolution of the wall-layer structures, as indicated by a large streak spacing, resulted in low wall stress and a high intercept of the logarithmic layer;[18] in calculations with the dynamic model no such phenomenon was observed. A possible explanation of the better accuracy achieved by the dynamic model in low-resolution calculation may be the less dissipative character of the model, compared with the Smagorinsky model, in the near-wall region. If the frequency and intensity of the large-scale bursting events is underestimated, so is the energy production associated with these events. Associated with bursting events is also

FIG. 8. Model coefficient and ratio of resolved turbulent stresses to large-scale turbulent kinetic energy. ——: Case 2; · · · ·: case 3. The dashed line represents a y^{+3} slope. (a) $\langle C\bar{\Delta}^2 \rangle$; (b) $\langle \mathscr{L}_{kk} \rangle / \langle q^2 \rangle$.
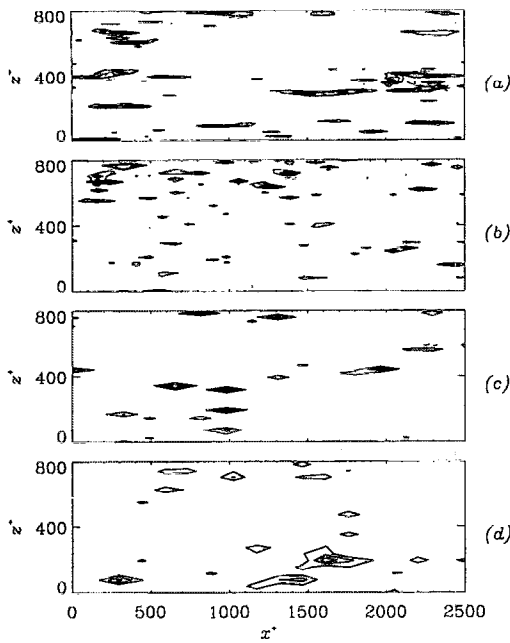
FIG. 10. Contours of large-scale Reynolds shear $u''v''$ in the $y^+ \approx 6$ plane. Dashed lines indicate positive contours. Contour levels are ± 2, ± 1.6, ± 1.2, ± 0.8, ± 0.4. (a) Case 1 ($\text{Re}_\tau = 200$); (b) case 2 ($\text{Re}_\tau = 1050$); (c) case 3 ($\text{Re}_\tau = 1050$); (d) case 4 ($\text{Re}_\tau = 2000$).

energy transfer from the small to the large scales[19] (subgrid-scale backscatter). In the near-wall region the dynamic model in the present formulation predicts much less subgrid-scale dissipation than the Smagorinsky model because the length scale is reduced due to the occurrence of local SGS backscatter (see below). A comparison of the length scales used in the dynamic model, $l_d = (C\bar{\Delta}^2)^{1/2}$, and in the Smagorinsky model, $l_s = 0.1\bar{\Delta}[1 - \exp(-y^+/25)]$ is shown in Fig. 11. The length scale l_s is almost ten times larger than l_d in the near-wall region, resulting in a subgrid-scale dissipation that is 100 times larger. Even if the damping function in the expression for l_s is changed to account for the near-wall behavior of τ_{12} as in Ref. 18, where the length scale used is $l_p = 0.1\bar{\Delta}[1 - \exp(-y^{+3}/25^3)]^{1/2}$, the Smagorinsky model remains more dissipative than the dynamic model.

Near the wall the length scale is essentially the same for cases 2 and 3. This is counterintuitive, since one would expect that, as the grid becomes coarser, the length scale representative of the subgrid scales should increase, and
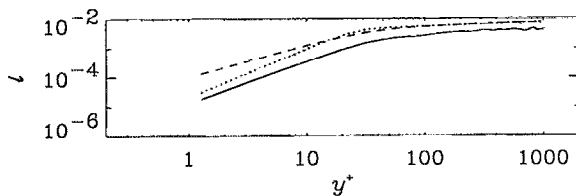

FIG. 11. Comparison of dynamic model and Smagorinsky model length scales. ———: l_d (dynamic model); — — —: l_s (Smagorinsky model); ····: l_p (Smagorinsky model with the correct near-wall asymptotic behavior).
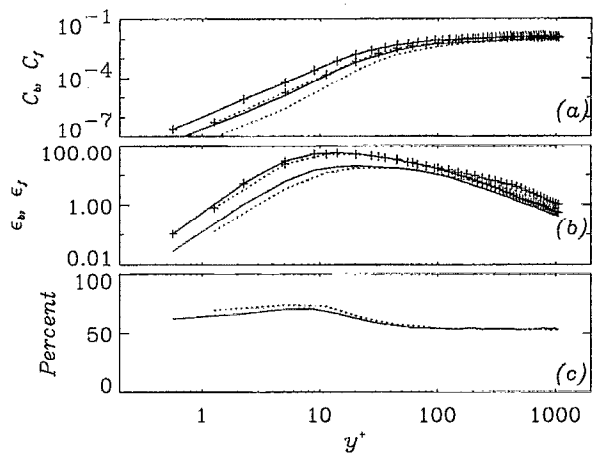

FIG. 12. Backward and forward contributions to the model coefficient and to the subgrid-scale dissipation. (a) Model coefficient. ———: $-C_b$, case 2; ····: $-C_b$, case 3; $+$ — $+$: C_f, case 2; $+\cdots+$: C_f, case 3. (b) SGS dissipation. ———: $-\epsilon_b$, case 2; ····: $-\epsilon_b$, case 3; $+$ — $+$: ϵ_f, case 2; $+\cdots+$: ϵ_f, case 3. (c) Percentage of points where $\mathscr{L}_{ij}M_{ij} > 0$. ———: case 2; ····: case 3.

can be explained by examining the model behavior in the near-wall region. Locally the quantity $\mathscr{L}_{ij}M_{ij}$, which appears in the numerator of (8), can be of either sign; on the average it is negative, and the coefficient C is positive, reflecting the fact that, on the average, small scales are dissipative even in the near-wall region. The effect of localized regions where $\mathscr{L}_{ij}M_{ij} > 0$, however, is to reduce the value of the coefficient and, therefore, the length scale, thereby accounting for subgrid-scale backscatter, albeit only in an average sense. To illustrate this point, in Fig. 12 are shown the positive and negative contributions to C, defined as

$$C_f = -\frac{1}{4}\frac{\langle \mathscr{L}_{ij}M_{ij} - |\mathscr{L}_{ij}M_{ij}|\rangle}{\langle M_{ij}M_{ij}\rangle},$$

$$C_b = -\frac{1}{4}\frac{\langle \mathscr{L}_{ij}M_{ij} + |\mathscr{L}_{ij}M_{ij}|\rangle}{\langle M_{ij}M_{ij}\rangle}. \tag{12}$$

The forward- and backward-scatter contributions to the SGS dissipation, $\epsilon_{\text{SGS}} = \tau_{ij}\bar{S}_{ij}$, are consequently given by

$$\epsilon_f = -C_f\bar{\Delta}^2|\bar{S}|^3, \quad \epsilon_b = -C_b\bar{\Delta}^2|\bar{S}|^3. \tag{13}$$

(This notation is different from the one used in Ref. 19, in which the backscatter was denoted by ϵ_+.) It can be seen from Fig. 12(a) that there is a substantial negative contribution to C across the channel, due to the fact that $\mathscr{L}_{ij}M_{ij} > 0$ at over 50% of the points [Fig. 12(c)]. This negative contribution is, effectively, a correction to the eddy viscosity, that is decreased due to local subgrid-scale backscatter. In the coarse-grid calculation, both positive and negative contributions to C in the near-wall region are substantially smaller than when the fine grid is used, but the positive and negative contributions to the SGS dissipation are similar [Fig. 12(b)], and the net SGS dissipation (not shown) is essentially the same for both calculations. In the near-wall region the percentage of points where $\mathscr{L}_{ij}M_{ij} > 0$ increases; SGS backscatter occurs at the same locations where the energy production is large, but the

average backscatter predicted by the model is not as high as expected based on the *a priori* results,[19] probably due to the less frequent occurrence of strong $u''v''$ events.

IV. CONCLUSIONS

The calculations presented here have demonstrated the applicability of the dynamic eddy viscosity model to high Reynolds number, wall-bounded flows. These were the first calculations in which flows at Reynolds numbers as high as $Re_c = 47\,100$ were simulated without resorting to wall functions or approximate boundary conditions.

The agreement between LES results and DNS and experimental data was very good. First and second moments of the velocity were predicted accurately, and higher moments (skewness and flatness) of the large-scale velocity were in fair agreement with the DNS and experimental data for the full velocity. The Reynolds number trends observed in experimental studies were reproduced by the LES; it is not yet clear, however, to what extent the resolution affects both the experimental and numerical data.

Although the model assumes that both test and grid cutoffs are in the inertial range, the results of the simulations are quite accurate even when the cutoff wave numbers are in the dissipation or energy-carrying regions of the spectrum.

The accuracy with which the wall-layer structures can be predicted depends strongly on the grid resolution: the streak spacing was overpredicted when coarse grids were used, and the structures appeared more diffuse, with fewer and weaker burst-type events. First- and second-order statistics, which may be the most important ones for engineering calculations, were predicted very accurately even when, as in cases 3 and 4, the streaks were not resolved.

One reason why the dynamic model can give good prediction of the first- and second-order moments, and fair prediction of higher moments even in the wall region, where the turbulent structures are not resolved, may be the fact that the eddy viscosity is reduced if subgrid-scale backscatter occurs with significant frequency. Although the model is based on a simple eddy viscosity assumption, it still represents forward and backward scatter (at least in an average sense). This may be one of the more positive features of the model.

The model is still lacking in that, in its present formulation, it cannot predict backscatter locally. As the grid is coarsened, both positive and negative contributions to the subgrid-scale dissipation are decreased; it is not clear, at this point, whether this feature is correct. Ideally, a model should be globally dissipative (to remove the energy that piles up near the cutoff wave number), but should also be able to account for the energy production associated with sweeplike and ejectionlike events that cannot be resolved by the mesh.

The dynamic model correctly predicts that energy transfer to the large scales is mainly associated with large-scale energy-producing events, and a local formulation, in which the coefficient is allowed to depend on all spatial coordinates and time, would account for the local backscatter more accurately than the present one, in which this effect is averaged over the entire plane. However, since the $u''v''$ events tend to be smeared by insufficient grid resolution, on coarse grids the very localized energy transfer to the large scales associated with these events might still not be predicted correctly, and the inclusion of a backscatter model might be desirable.

[1] U. Piomelli, "Applications of large-eddy simulation in engineering: an overview," in *Large Eddy Simulation of Complex Engineering and Geophysical Flows*, edited by B. Galperin and S. A. Orszag (Cambridge University Press, Cambridge, 1993).

[2] M. Germano, U. Piomelli, P. Moin, and W. H. Cabot, "A dynamic subgrid-scale eddy viscosity model," Phys. Fluids A **3**, 1760 (1991).

[3] S. Ghosal, T. S. Lund, and P. Moin, "A local dynamic model for LES," *Annual Research Briefs 1992* (Center for Turbulence Research, Stanford University, Stanford, CA, 1993), p. 3.

[4] R. Garg and U. Piomelli, "Large-eddy simulation of detuned transition," in Proceedings of the 4th International Symposium on Computational Fluid Dynamics, Davis, California, 1991.

[5] P. Moin, K. Squires, W. H. Cabot, and S. Lee, "A dynamic subgrid-scale model for compressible turbulence and scalar transport," Phys. Fluids A **3**, 2746 (1991).

[6] W. H. Cabot and P. Moin, "Large eddy simulation of scalar transport with the dynamic subgrid-scale model," in Ref. 1.

[7] D. K. Lilly, "A proposed modification of the Germano subgrid-scale closure method," Phys. Fluids A **4**, 633 (1992).

[8] V. C. Wong, "A proposed statistical dynamic closure method for the linear or nonlinear subgrid-scale stresses," Phys. Fluids A **4**, 1080 (1992).

[9] C. Ronchi, M. Ypma, and V. M. Canuto, "On the application of the Germano identity to subgrid scale modeling," Phys. Fluids A **4**, 2927 (1992).

[10] U. Schumann, "Subgrid scale model for finite difference simulation of turbulent flows in plane channels and annuli," J. Comput. Phys. **18**, 376 (1975).

[11] U. Piomelli, J. Ferziger, P. Moin, and J. Kim, "New approximate boundary conditions for large eddy simulations of wall-bounded flows," Phys. Fluids A **1**, 1061 (1989).

[12] M. Germano, "Turbulence: the filtering approach," J. Fluid Mech. **238**, 325 (1992).

[13] T. A. Zang and M. Y. Hussaini, "On spectral multigrid methods for the time-dependent Navier–Stokes equations," Appl. Math. Comp. **19**, 359 (1986).

[14] J. Kim, P. Moin, and R. Moser, "Turbulence statistics in fully developed channel flow at low Reynolds number," J. Fluid Mech. **177**, 133 (1987).

[15] T. Wei and W. W. Willmarth, "Reynolds-number effects on the structure of a turbulent channel flow," J. Fluid Mech. **204**, 57 (1989).

[16] J.-L. Balint, J. M. Wallace, and P. Vukoslavčević, "The velocity and vorticity vector fields of a turbulent boundary layer. Part 2. Statistical properties," J. Fluid Mech. **228**, 53 (1991).

[17] R. B. Dean, "Reynolds number dependence of skin friction and other bulk flow variables in two-dimensional rectangular duct flow," J. Fluids Eng. **100**, 215, (1978).

[18] U. Piomelli, P. Moin, and J. H. Ferziger, "Model consistency in large eddy simulation of turbulent channel flows," Phys. Fluids **31**, 1984, (1988).

[19] U. Piomelli, W. H. Cabot, P. Moin, and S. Lee, "Subgrid-scale backscatter in turbulent and transitional flows," Phys. Fluids A **3**, 1766 (1991).